CHINESE OPTICS LETTERS

Vol. 24, No. 6 | June 2026

Simultaneous sorting of fractional vortex beams based on diffractive optical neural network

Shiyong Ren (任仕勇)[1,†], Yuhan Jiao (焦雨菡)[1,†], Fangkui Sun (孙芳魁)[1*], Qi Jia (贾 琦)[1,2**], Rui Feng (冯 睿)[1], Yongyin Cao (曹永印)[1], Jian Wang (王 健)[3], Yongkang Dong (董永康)[4], Hongyan Shi (时红艳)[3], and Weiqiang Ding (丁卫强)[1,5***]

[1] Institute of Advanced Photonics, School of Physics, Harbin Institute of Technology, Harbin 150001, China

[2] School of Materials Science and Engineering, Harbin Institute of Technology, Harbin 150001, China

[3] School of Physics, Harbin Institute of Technology, Harbin 150001, China

[4] School of Astronautics, Harbin Institute of Technology, Harbin 150001, China

[5] Collaborative Innovation Center of Extreme Optics, Shanxi University, Taiyuan 030006, China

[†]These authors contributed equally to this work.

*Corresponding author: fksun@hit.edu.cn

**Corresponding author: jiaqi1350@hit.edu.cn

***Corresponding author: wqding@hit.edu.cn

Received November 17, 2025 | Accepted January 26, 2026 | Posted Online June 9, 2026

Fractional vortex beams (FVBs), endowed with unique and complex optical field distributions, exhibit superior potential compared to integer vortex beams in diverse fields such as optical communications. Consequently, the accurate and high-quality sorting of FVBs is of paramount importance. However, traditional methods struggle to meet the stringent requirements for efficiency, crosstalk, and resolution in FVB sorting. Meanwhile, although diffractive optical neural networks (DONNs) have been successfully applied to integer-order orbital angular momentum (OAM) sorting, their application in the non-integer domain remains unexplored. In this paper, we systematically demonstrate the complete workflow and potential efficacy of DONNs in addressing the specific challenges of FVB sorting for the first time. In simulations, we achieve inter-channel crosstalk below −20 dB. Meanwhile, we elaborate on the precise OAM spectrum measurement capability of DONNs and successfully employ DONNs to experimentally measure the spectral distributions of different OAM states for the first time, achieving a measurement fidelity of approximately 99%. This provides a novel all-optical measurement approach for the quantitative evaluation of OAM spectra. Furthermore, we integrate FVB sorting with wavelength-division multiplexing (WDM) technology, enabling our sorting device to maintain stable performance at two wavelengths (532 nm and 660 nm) with an experimental output crosstalk below −10 dB. We believe that this rapid sorting method, which combines the high-speed operation, high efficiency, and high parallelism of optical neural networks, holds tremendous potential for future high-dimensional optical communications, optical metrology, and so on.

Keywords: diffractive optical neural network; fractional vortex beam; dual-wavelength wavelength division multiplexing; OAM spectrum measurement.

© The Authors. Published by Chinese Laser Press under a Creative Commons Attribution 4.0 International License. Distribution or reproduction of this work in whole or in part requires full attribution of the original publication, including its DOI.

DOI: 10.3788/COL202624.061102

1. Introduction

Following the initial proposal of vortex beams by Allen *et al.*[1], researchers have discovered a wide variety of beams carrying optical vortices, which hold significant potential in both theoretical and practical applications[2]. Nowadays, orbital angular momentum (OAM) beams have been widely adopted in various applications with unprecedented performances, including high-capacity optical communications[3–9], optical manipulation[10–13], super-resolution microscopy[14,15], optical metrology[16], and high-dimensional quantum states[17–19].

Compared to integer-order optical vortices, fractional vortex beams (FVBs) possess unique radial intensity nulls, enabling finer intensity distribution control—a characteristic that yields richer spatial details and higher information density. This property directly enhances optical force precision for particle manipulation[20], and it further extends their advantages to applications requiring complex structured light field engineering, such as cell sorting[21,22]. In the realm of optical imaging, FVBs can achieve anisotropic edge enhancement, in contrast to integer vortex beams, which only provide isotropic edge enhancement[23–25]. Additionally, FVBs offer more degrees of freedom and combinations, significantly increasing the capacity of communication channels and improving data transmission efficiency[26,27]. These unique advantages have propelled FVBs to the forefront of contemporary photonics research.

To fully leverage the advantages of FVBs, accurate sorting and measurement methods are crucial. Currently, researchers have developed various methods and techniques for the precise sorting of vortex beams. However, their extension from integer-order vortices to FVBs often falls short of expectations. For example, due to the lack of orthogonality between fractional OAM modes, traditional forked grating methods—originally designed for integer OAM—tend to exhibit poor resolution and high intermodal crosstalk when applied to FVB sorting[28,29]. Additionally, geometric-phase-based transformation methods, which convert the helical phase profile of vortex beams into transverse linear phase gradients, face challenges in sorting FVBs due to the increased spatial overlap of the resulting focused spots[30,31]. In 2014, Zhang *et al.* used a Dove prism and a polarizing beam splitter to transform the separation of different OAM states of vortex light into odd–even mode separation, successfully achieving the sorting of FVBs for the first time[32]. Unfortunately, their OAM sorting system with multiple cascaded units is complex, making it challenging to scale up for sorting a larger number of modes. Recently, metasurfaces have emerged as an innovative platform for sorting vortex light fields[33]. The method described in Ref. [33] successfully demonstrates the feasibility of this approach using a single-layer design. However, in practical applications, metasurfaces may require more complex structural designs (such as multi-layer diffractive structures) to further enhance functionality[34]. A key challenge at this stage lies in the precise calibration of the subwavelength features within these diffractive layers, which can impose constraints on the further development of advanced functionalities.

Noticeably, diffractive optical neural networks (DONNs) have emerged as a transformative platform for optical computing[35,36] and optical field manipulation[37–44]. While previous DONN studies demonstrated integer vortex beam (de)multiplexing[38–40] and OAM sorting[41,42], their applicability to FVBs remains unexplored. This work represents a further in-depth study and an extension of our previous research[43] on DONN-based vortex beam sorting, incorporating multi-wavelength theoretical and experimental extension, precise measurement of the OAM spectrum, further matching of experiment and simulation, and so on. In this work, we propose an FVB sorter based on a DONN, leveraging deep-learning-optimized phase modulation to extend the DONN's applicability for mode multiplexing and completing a full cycle from theoretical design and simulation optimization to experimental validation. We experimentally demonstrated this sorter for eight FVBs, obtaining results consistent with theoretical predictions. Additionally, OAM spectrum measurements performed with our system were characterized by a high precision of 99%. It demonstrates a novel all-optical measurement approach for the quantitative evaluation of OAM spectra. Furthermore, we extend the sorter's functionality by implementing dual-wavelength wavelength-division multiplexing (WDM), and similarly, the experimental results obtained were in complete agreement with the theoretical expectations. Experimental validation shows <-10 dB inter-channel crosstalk for 8 FVBs, with dual-wavelength WDM extension maintaining performance at 532 nm and 660 nm. This approach unlocks the full potential of FVBs in applications requiring fractional OAM states, paving the way for novel developments in optical technologies.

2. Principle and Methods

For the selection of beams in the training set, the Laguerre–Gaussian (LG) beam, as a typical representative of vortex beams, is chosen as the input beam for our training. Under the paraxial approximation, its expression in cylindrical coordinates is given by

$$\begin{aligned} \mathrm{LG}_m^p(r,\varphi,z) = {} & \frac{C_m^p}{\omega(z)}\left(\frac{r\sqrt{2}}{\omega(z)}\right)^{|m|} L_p^{|m|}\left(\frac{2r^2}{\omega(z)^2}\right) \\ & \times \exp\left(\frac{-\mathrm{j}kr^2 z}{2(z^2+z_R^2)}\right)\exp(\mathrm{j}m\varphi) \\ & \times \exp(\mathrm{j}(2p+|m|+1)\psi(z)). \end{aligned} \tag{1}$$

In the equation, z is the propagation distance; $k=2\pi/\lambda$ is the wave number; p represents the radial index; $z_R=\pi\omega_0^2/\lambda$ is the Rayleigh length, $\psi(z)$ is the azimuthal angle, $\psi(z)=\arctan(z/z_R)$; $\omega(z)$ is the waist size at the beam's focus, $\omega(z)=\omega_0\sqrt{1+(z/z_R)^2}$; C_m^p is the normalized amplitude coefficient; and $L_p^{|m|}$ is the associated Laguerre polynomial, expressed as

$$L_p^{|m|}(x)=\sum_{n=0}^{p}(-1)^n\frac{(|m|+p)!}{(p-n)!(|m|+n)!n!}x^n. \tag{2}$$

For the sorting of FVBs, we pay special attention to half-integer vortices, which can be realized by attaching a half-integer vortex phase to an integer-order LG beam[32]:

$$\begin{cases} \mathrm{LG}_l^p = \mathrm{LG}_m^p \exp\left(-\mathrm{j}\frac{1}{2}\varphi\right) & m>0 \\ \mathrm{LG}_l^p = \mathrm{LG}_m^p \exp\left(\mathrm{j}\frac{1}{2}\varphi\right) & m<0 \end{cases}, \tag{3}$$

where l represents the OAM value carried by the half-integer vortex beam.

Next, to correctly sort the input FVBs, it is essential to understand the architecture of the DONN and the optical field propagation process to design its diffractive layer structure. The DONN framework proposed in Ref. [37] comprises a series of optically interconnected diffractive layers. These layers contain predefined neurons whose parameters are iteratively trained to implement specific target functions. In this section, we derive the DONN training details, based on the error backpropagation algorithm. It is worth mentioning that, since the size of the neuron we designed is 8 μm, its characteristic size is much larger than the wavelength of the training light; therefore, we use the angular spectrum theory to calculate the propagation of light. According to angular spectrum theory[45], an optical field's propagation can be described by decomposing the field into its spatial frequency components as

$$U(x,y,z)=\mathcal{F}^{-1}\{\mathcal{H}(f_x,f_y,z)\mathcal{F}(U(x,y,0))\}, \tag{4}$$

where $\mathcal{F}$ represents the two-dimensional Fourier transform, $\mathcal{F}^{-1}$ represents the two-dimensional inverse Fourier transform, and $\mathcal{H}$ is the transfer function, which can be expressed as

$$\mathcal{H}=\begin{cases}\exp\left(\mathrm{j}kz\sqrt{1-(\lambda f_x)^2-(\lambda f_y)^2}\right) & f_x^2+f_y^2\le 1/\lambda^2\\ 0 & f_x^2+f_y^2>1/\lambda^2\end{cases}, \tag{5}$$

where f_x and f_y denote the spatial frequencies of plane light within the spatial bases x and y, respectively. We define $\mathcal{D}=\mathcal{F}^{-1}\mathcal{H}\mathcal{F}$ as the diffraction operator, which computes the propagation of light waves between adjacent layers. After free-space propagation, the light field is modulated by the neurons on the next diffractive layer, and the resulting field then undergoes free-space propagation again. Incorporating this modulation Eq. (4) yields

$$U(x,y,z)=\mathcal{F}^{-1}\{\mathcal{H}\mathcal{F}(TU(x,y,0))\}=\mathcal{D}TU(x,y,0), \tag{6}$$

where $T=\exp(\mathrm{j}\varphi)$ is the complex transmission coefficient of the neuron on the diffractive layer. At this point, we obtain the forward propagation model of the diffractive neural network:

$$\begin{cases}X_{\zeta+1}^{\gamma}=\mathcal{F}^{-1}\{\mathcal{H}\mathcal{F}(T_{\zeta}^{\gamma}X_{\zeta}^{\gamma})\}=\mathcal{D}T_{\zeta}^{\gamma}X_{\zeta}^{\gamma}\\ T_{\zeta}=\exp(\mathrm{j}\varphi_{\zeta})\end{cases}, \tag{7}$$

where X_{ζ}^{γ} represents the complex amplitude distribution of the optical field at the γth sample on the ζth diffractive layer, T_{ζ} is the complex transmission coefficient of the neuron on the ζth diffractive layer, φ_{ζ} denotes the phase delay of the neuron on the ζth diffractive layer, and there are a total of N_d diffractive layers. This discretization does not affect the generality of our approach, provided that the spatial sampling interval (i.e., pixel pitch) remains much smaller than the characteristic transverse field feature size, as explained earlier using the angular spectrum theory. Since our work requires measuring the light intensity in the detection region on the output plane, without considering the phase distribution on the output plane, we use the mean squared error (MSE) of the light intensity as the loss function for training our network:

$$\mathcal{L}=\frac{1}{N_t}\sum_{\gamma=1}^{N_t}(I_{\mathrm{tar}}^{\gamma}-I^{\gamma})^2, \tag{8}$$

where $I_{\mathrm{tar}}^{\gamma}$ and $I^{\gamma}=(X_{\mathrm{out}}^{\gamma})^{*}X_{\mathrm{out}}^{\gamma}$ represent the preset light intensity and the actual light intensity distribution on the output plane for the γth sample, respectively; N_t is the total number of samples. For an N_d-layer diffractive layer, $X_{\mathrm{out}}^{\gamma}=X_{N_d+1}^{\gamma}$. During training, we use the stochastic gradient descent (SGD) algorithm to update the parameters. The gradient of the loss function $\mathscr{L}$ with respect to the phase φ_{ζ} is given as follows:

$$\begin{cases}\frac{\partial\mathcal{L}}{\partial\varphi_{\zeta}}=-\frac{1}{N_t}\sum_{\gamma=1}^{N_t}\frac{\partial\mathcal{L}}{\partial I^{\gamma}}\frac{\partial I^{\gamma}}{\partial X_{\mathrm{out}}^{\gamma}}\frac{\partial X_{\mathrm{out}}^{\gamma}}{\partial\varphi_{\zeta}}+\mathrm{c.c.}\\ \quad=-\frac{2}{N_t}\sum_{\gamma=1}^{N_t}\mathrm{Re}\left(\frac{\partial\mathcal{L}}{\partial I^{\gamma}}\frac{\partial I^{\gamma}}{\partial X_{\mathrm{out}}^{\gamma}}\frac{\partial X_{\mathrm{out}}^{\gamma}}{\partial\varphi_{\zeta}}\right)\\ \frac{\partial X_{\mathrm{out}}^{\gamma}}{\partial\varphi_{\zeta}}=\mathcal{D}\varphi_{N_d}\mathcal{D}\varphi_{N_d-1}\cdots\frac{\partial\mathcal{D}\varphi_{\zeta}X_{\zeta}^{\gamma}}{\partial\varphi_{\zeta}}\end{cases}, \tag{9}$$

where Re(·) denotes the real part operator. In summary, we have derived the forward and backward propagation models of the entire network. Based on Eqs. (7)–(9), the DONN is trained to obtain the phase distribution of the diffractive layers.

3. Results

3.1. Single-wavelength FVB sorting results

Here, we illustratively demonstrate eight information channels to showcase the design principle, and this design strategy can be extended to detect more OAM states. Accordingly, we selected eight FVBs as input beams with $l=-3.5$ to 3.5 ($\Delta l=1$). For the target output, we chose Gaussian beams with a small waist, located at positions corresponding to the index l of the input FVBs. The training results of the DONN are closely related to the network parameters and training settings. Throughout the training simulation process, we used a light wavelength of 660 nm and configured four diffractive layers. Each diffractive layer contains 400×400 neurons, with an inter-layer distance of 29.5 mm and a distance of 72 mm from the last diffractive layer to the output plane. The size of the neurons on each layer matches the pixel size of the spatial light modulator, set to 8 μm. The optimizer employed is the Adam optimizer with a momentum coefficient of (0.9, 0.999); the network uses the MSE of the light intensity to quantify the difference between the target and the actual output; the neuron parameters are updated using the SGD algorithm. Here, the numerical simulation is implemented on the platform of Python version 3.13.2 with PyTorch framework version 2.6.0 using a desktop computer (NVIDIA GeForce 2080 SUPER GPU, Intel Core i7 12700 CPU at 2.10 GHz with 12 cores, and 32 GB of RAM, running with a Microsoft Windows 10 operating system). The conceptual diagram of our FVB sorting device is shown in Fig. 1(a). By establishing a one-to-one correspondence between the incident vortex light and Gaussian

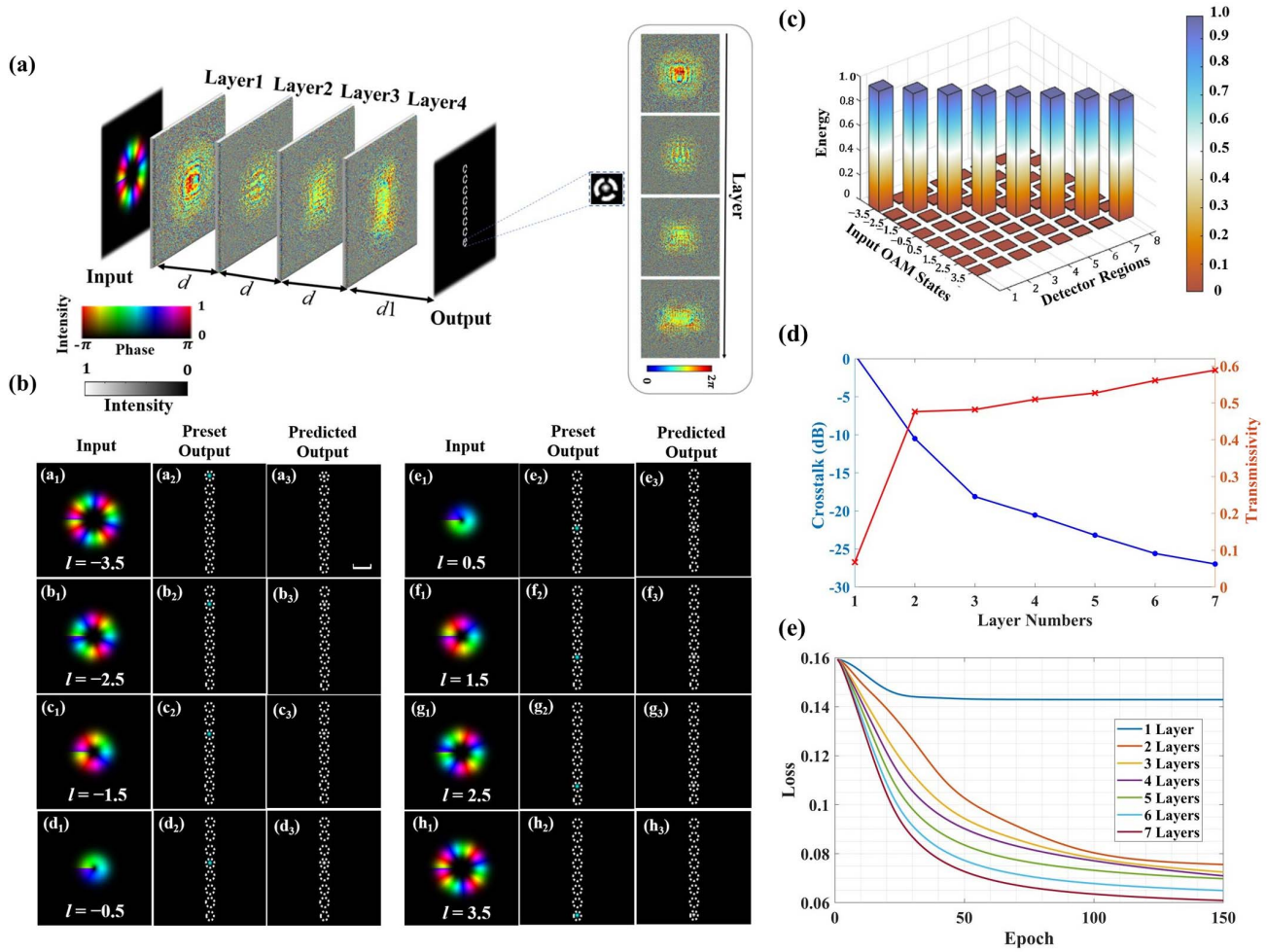

Fig. 1. (a) Training architecture of the DONN and the phase distribution of the diffractive layers. The inter-layer distance d is 29.5 mm, and the distance d_1 between the diffractive layer and the output plane is 72 mm. (b) Sorting results of the 8 FVBs (scale bar: 200 μm). Panels (a_1)–(h_1) show the input field distribution, panels (a_2)–(h_2) represent the preset target intensity distribution, and panels (a_3)–(h_3) illustrate the actual output intensity distribution of the trained network. (c) Normalized energy distribution histogram on the output plane of the validation set. (d) Curve showing how the network output crosstalk and transmissivity vary with the number of diffractive layers. (e) Loss function curves of the network with different diffractive layers.

beams at different channel positions on the output plane, the identification and sorting of different OAM states are converted into measuring the energy levels in various detection channels on the output plane.

For a given input, the sorting is considered successfully when the output signal is accurately assigned, resulting in a total intensity at the target detection area corresponding to the input that is significantly greater than the intensity in other detection areas. For any input $|\psi_{\text{in}}\rangle$ ($l = -3.5$ to 3.5, $\Delta l = 1$) in the training set, the maximum optical intensity on the output plane is evenly distributed at the corresponding target positions. Figure 1(b) presents the corresponding sorting results. In Fig. 1(b), panels (a_1) to (h_1) show the light field distribution on the input plane, panels (a_2) to (h_2) represent our preset target intensity distributions, and panels (a_3) to (h_3) illustrate the actual output intensity distributions of the trained network. To provide a more intuitive view of the output sorting results, Fig. 1(c) plots the normalized energy distribution histogram across detection channels for a single FVB input, demonstrating minimal energy crosstalk below −20 dB between channels.

Generally, an increase in the number of diffractive layers can effectively improve the degree of freedom of phase modulation and the precision of optical field regulation. To verify this, we calculate the crosstalk and the transmissivity as a function of the number of diffractive layers, as shown in Figs. 1(d) and 1(e). We define them as follows:

$$\begin{cases} W = 10 \times \lg\left(\dfrac{\sum_{\alpha,\beta(\alpha\neq\beta)} I_{\alpha,\beta}}{I_{\alpha,\alpha}}\right), \\ \text{Tr} = \dfrac{\sum_s I_s}{I_{\text{in}}} \end{cases} \tag{10}$$

where $I_{\alpha,\beta}$ represents the energy corresponding to channels other than the output channel for the input signal, and $I_{\alpha,\alpha}$ represents the energy on the output channel corresponding to the

input signal. I_{in} denotes the total input energy, and I_s denotes the energy of the sth detection region on the output plane.

As shown in Fig. 1, a larger number of diffractive layers leads to a faster convergence speed and a better convergence effect of the network loss function, and the sorting crosstalk on the output plane gradually decreases and tends to saturation accordingly. Meanwhile, the effective transmissivity of the network output plane increases progressively, which indicates that more energy of the incident optical field is accurately allocated to the target detection regions. It is worth noting that, although increasing the number of diffractive layers can enhance the modulation performance of the network, in practical applications, an excessive number of diffractive layers greatly increases the fabrication cost of the device and the difficulty of optical path alignment. Therefore, it is necessary to seek an optimal balance between the system performance and practical application cost. As shown in the simulation results, when the number of diffractive layers exceeds 4, the reduction rate of sorting crosstalk is less than 12% and basically reaches saturation at approximately 6 layers; the increase rate of effective transmissivity is also lower than 3.3%. Based on this, a four-layer diffractive structure is finally selected as the optimal scheme in this study, which achieves a favorable balance between the sorting performance and system complexity.

To verify the practical application of our designed FVB sorting device, we constructed a corresponding experimental system, as illustrated in Fig. 2. The laser source emits a stable beam at a wavelength of 660 nm. $Lens_1$ and $Lens_2$ are used for beam expansion and collimation, while $Lens_3$ and $Lens_4$ form a 4-f imaging system with an aperture stop to eliminate stray light. A non-polarizing beam splitter (NPBS) is used to reflect the collimated light onto SLM_1 (Holoeye PLUTO-2-VIS-016). Liquid-crystal spatial light modulator (LC-SLM) technologies have been regarded as versatile tools for generating arbitrary optical fields[46]. When the laser beam is incident on the SLM loaded with different helical phase structures, vortex beams with different OAM states will be generated. Details on image loading are provided in the Supplementary Material. In our setup, after passing through $Lens_1$ and $Lens_2$ and a polarizer, the beam is converted into horizontally polarized light to match the modulation requirement of the SLM. It then impinges on SLM_1 (Holoeye PLUTO-2-VIS-016), which is loaded with different helical phase structures to generate vortex beams with various OAM states, thereby producing the FVBs that serve as inputs to the subsequent DONN. Finally, SLM_2 (Holoeye PLUTO-BB) is divided into four regions to load the diffractive layer phases obtained from simulations. The beam undergoes continuous modulation by passing through these four diffractive layers via back-and-forth reflections facilitated by a mirror. The resulting output is captured by a charge-coupled device (CCD) camera and displayed on a computer monitor. For such multilayer diffractive structures, the alignment accuracy between individual layers during experimental testing poses a significant impact on the neural network's output. This primarily comprises axial and radial alignment, and further information on the alignment process of the DONN can be found in our earlier work[47].

Figure 3 shows the experimental sorting results for single and multimode superimposed FVB inputs. Figure 3(a) presents the CCD images captured for eight distinct single FVBs with a specified OAM interval of $\Delta l = 1$. It is evident that our sorting device successfully sorts the different FVBs into their corresponding target areas, completely aligning with theoretical expectations. Figure 3(b) provides a more intuitive display of the sorting results for the eight single-mode FVB inputs, achieving an accuracy of 100%. In Fig. 3(c), panels (a_1), (b_1), and (c_1) show the

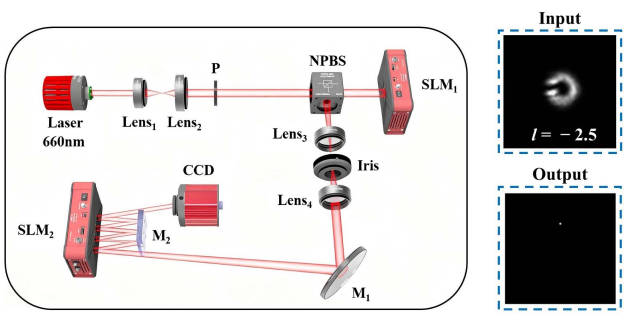

Fig. 2. Schematic diagram of the experimental setup for FVB sorting using the DONN. The Gaussian laser beam with a wavelength of 660 nm is expanded and collimated by $Lens_1$ and $Lens_2$ and followed by a polarizer P. $Lens_1$ and $Lens_2$ form a beam expander for modulation by SLM_1, where different FVBs are generated as inputs for the DONN. $Lens_3$ and $Lens_4$ form a 4-f system with an aperture stop to filter stray light. SLM_2, divided into four regions, loads simulation-derived diffractive layers, modulating the beam via reflections. The final output is captured by a CCD and displayed on a monitor.

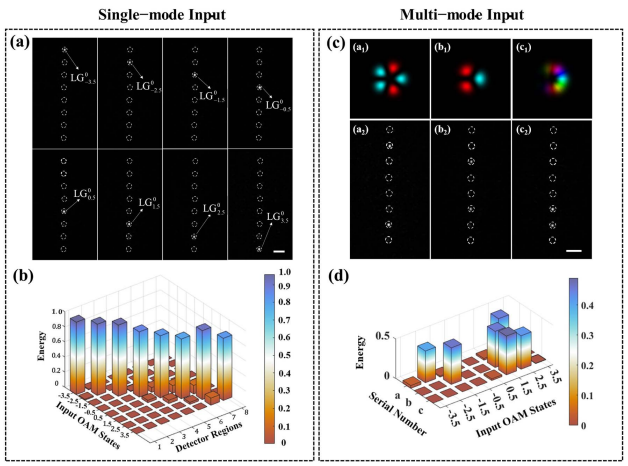

Fig. 3. Experimental sorting results of 8 FVBs. (a) Input single-mode FVBs and their corresponding output intensity distributions. (b) Normalized intensity distribution histogram of the output surface for single-mode FVB input. (c) Input of multimode FVBs and their corresponding output intensity distributions. Among them, panels (a_1)–(c_1) represent three groups of superimposed FVBs input optical fields. Panels (a_2)–(c_2) represent the corresponding output images received by the CCD for each case. (d) is the normalized energy distribution histogram of the output area for the input optical field in (c). Scale bars: 200 μm.

RGB images of the input complex amplitudes of the input optical fields: $|\psi_{\text{in}}\rangle = |\text{LG}^0_{-2.5}\rangle + |\text{LG}^0_{2.5}\rangle$, $|\psi_{\text{in}}\rangle = |\text{LG}^0_{-1.5}\rangle + |\text{LG}^0_{1.5}\rangle$, and $|\psi_{\text{in}}\rangle = |\text{LG}^0_{1.5}\rangle + |\text{LG}^0_{2.5}\rangle$. Fig. 3(c) panels ($a_2$), ($b_2$), and ($c_2$) represent the corresponding experimental output intensity distributions recorded by the CCD. It is evident that these output results match the target receiving areas precisely. We normalized the total energy, and the energy distribution across different regions is depicted in Fig. 3(d). As expected, the inter-channel crosstalk remains very low, consistent with our design requirements.

It is noteworthy that, to realize such high-precision performance in practice, it is essential to address the performance gap between simulated phase masks and real-world optical systems—a challenge commonly referred to as the "realism gap" in DONN-based designs[48]. Although an *in situ* training method for the DONN has been proposed to iteratively update the hardware[49,50], this approach necessitates the detection of the output and input lights of each layer, which is challenging to implement in our experimental system. Here, to address this challenge, we introduced Gaussian convolution kernels during both the forward and backward propagation phases of the simulation process. This was done to apply convolution smoothing to the diffractive layer's phase, which helps reduce discrepancies caused by the limitations of the SLM's modulation capabilities. In addition, we also found that using Gaussian convolution for smoothing has a certain degree of robustness to layer misalignment. The specific results can be found in Note 2 of the Supplementary Material.

3.2. Multi-wavelength FVB sorting results

In prior work, the architecture of multi-wavelength DONN has been proposed[51,52]. Here, to fully leverage the parallel capabilities of the DONN, we also developed a multi-wavelength DONN to sort FVBs across multiple wavelengths. We modified the loss function to account for the input light wavelength, yielding

$$\mathcal{L} = \frac{1}{N_t}\sum_{\gamma,\lambda} w_\lambda (I^{\gamma,\lambda}_{\text{tar}} - I^{\gamma,\lambda})^2 = w_{\lambda_1}\mathcal{L}_{\lambda_1} + w_{\lambda_2}\mathcal{L}_{\lambda_2} + \cdots + w_{\lambda_n}\mathcal{L}_{\lambda_n}, \tag{11}$$

where $I^{\gamma,\lambda}_{\text{tar}}$ and $I^{\gamma,\lambda}$ denote the target and actual outputs of sample γ at the wavelength λ, respectively. Multi-wavelength sorting is optimized by adjusting the weights w_λ of the per-wavelength loss functions. Note that, due to dispersion effects, optimal performance requires characterizing the phase modulation response of the SLM at each wavelength. In practical training—reflecting our experimental setup—we selected light wavelengths of 532 nm and 660 nm for simulation and measurement. First, we calibrated the SLM at 660 nm, ensuring linear modulation from 0 to 2π. Using this as a reference, we then measured the SLM modulation curve for 532 nm light. For more details, see Note 1 of the Supplementary Material. Given the application of wavelength-division multiplexing (WDM), we defined two wavelength channels (left and right) on the output plane. As in the single-wavelength FVB sorting, we employed four diffractive layers for training, with the neuron count and size per layer as described in Fig. 1(a).

We present the training results for the multi-wavelength sorting network in Fig. S7 in the Supplementary Material. The output plane is divided into two wavelength channels (left and right), with each channel set to have six different detection areas, corresponding to six distinct FVB inputs. For light inputs of different wavelengths, the final sorting results appear in the respective wavelength channels. In Fig. S7 (Supplementary Material), panels (a_1) to (a_6) and (f_1) to (f_6) represent the spatial light field distributions of 532 nm and 660 nm wavelength inputs, respectively; panels (b_1) to (b_6) and (e_1) to (e_6) depict the target output spatial light field distributions for 532 nm and 660 nm wavelengths; panels (c_1) to (c_6) and (d_1) to (d_6) show the predicted output spatial light field distributions for 532 nm and 660 nm wavelengths after passing through the trained network. As evident from the results, our network not only accomplishes wavelength separation but also successfully sorts the FVBs. Following transmission through the designed network, light of distinct wavelengths is accurately separated on the output plane. Moreover, the signal interference among channels is negligible, demonstrating a high sorting quality.

We also conducted necessary experimental validations to demonstrate the efficiency of the multi-wavelength FVB sorting device we trained earlier. The experimental setup used is consistent with that shown in Fig. 2. It is particularly noteworthy that switching the operating wavelength does not necessitate recalibration of the phase modulation patterns on the SLM. This capability stems from the integration of a wavelength-to-phase response mapping model during the network training phase. Through a joint optimization algorithm, this mapping is embedded into the network parameters during simulation, enabling parallel adaptation to the dual-trained wavelengths (532 nm and 660 nm) for input conditions. As a result, the system achieves efficient dual-band operation. And the phase modulation patterns loaded on the SLM remain unchanged for the two trained wavelengths, significantly enhancing its reconfigurability and practical utility. This advancement paves the way for broader application of such devices in multi-wavelength optical computing systems.

Figure 4 shows the final experimental results. The output plane features Gaussian beams corresponding to different detection areas. In Fig. 4, panels (c_1) to (h_1) show the output field distribution when single-mode vortex beams at a wavelength of 532 nm are incident, while panels (c_2) to (h_2) display the output field distribution for single-mode vortex beams at a wavelength of 660 nm. The output regions for both wavelengths are configured as set in the simulations, divided into left and right wavelength channels. It is evident that altering the wavelength of the incident light allows the same FVBs to be sorted into different channels. This observation aligns perfectly with our initial expectations and highlights the versatility of our sorting device. Such functionality is crucial for applications in WDM, particularly in the realm of optical communications, where efficient sorting and routing of various signal types are essential for enhancing data transmission capacity and improving overall

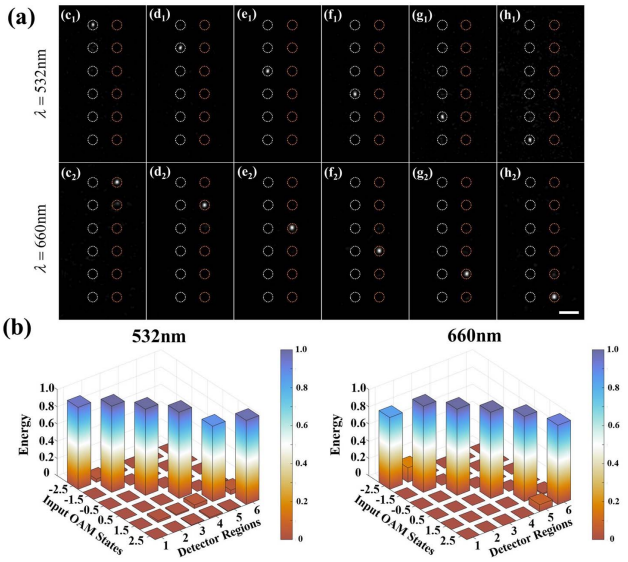

Fig. 4. Experimental results of multi-wavelength FVB sorting. (a) Output optical field distributions for single-mode inputs at different wavelengths (scale bar: 200 μm). Panels (c_1)–(h_1) display the corresponding output plane intensity distributions for single-mode FVBs input at 532 nm, while panels (c_2)–(h_2) show the corresponding output plane intensity distributions for single-mode FVBs input at 660 nm. (b) Histograms of the light intensity energy distribution in the detection regions on the output plane for single-mode inputs at 532 nm and 660 nm wavelengths.

system performance. As previously noted, we selected two wavelengths, 532 nm and 660 nm, to validate the network's multi-wavelength parallel functionality. However, this choice does not constrain the network's optical field manipulation capability to only these wavelengths; by incorporating additional wavelength channels during training, its full potential for parallel optical field control can be realized.

4. Discussion

Accurate measurement of the OAM spectrum is essential for evaluating the quality of generated beams, analyzing crosstalk between modes, and optimizing OAM-based systems. This process typically involves detecting the distribution of energy across different OAM modes to ensure precise identification and sorting of OAM states.

Since vortex beams with different OAM values are mutually orthogonal, they can serve as a set of orthogonal basis functions for representing and analyzing other vortex beams. By projecting an unknown vortex beam onto these orthogonal bases, it is possible to determine its OAM spectrum through energy measurements. In our simulations and experiments, we selected the eight vortex beams with $l = -3.5$ to 3.5 as the orthogonal bases and measured the output OAM spectra of the seven beams with $m = -3$ to 3. This characterization can be achieved by measuring the energy distribution of the different OAM channels on the output plane upon incidence. Mathematically, a given vortex beam can be represented as a linear combination of the orthogonal basis functions:

$$|\mathrm{LG}_m^p\rangle = \sum_l c_l |\mathrm{LG}_l^p\rangle, \tag{12}$$

where c_l represents the projection coefficients of the input vortex beam onto the different orthogonal bases and $c_l = \langle \mathrm{LG}_m^p | \mathrm{LG}_l^p \rangle$ denotes the orthogonal basis functions.

Based on the fundamental principle of modal decomposition, the energy phenomenon observed in non-adjacent OAM vortex beam channels can be reasonably explained. The mathematical foundation lies in the basis transformation: an optical field composed of integer-order OAM eigenstates can be projected onto a complete orthogonal basis set of half-integer-order OAM for analysis. Under this projection, although the optical field exhibits its high purity in its original integer-order modes, within the half-integer-order basis set, theoretically, besides the two adjacent half-integer-order modes accounting for the majority of the energy, all other fundamental modes must possess non-zero projection coefficients. Our numerical simulations and experimental results confirm this theoretical expectation, demonstrating that, despite the high energy concentration in adjacent channels, projections onto non-adjacent channels indeed exist, which is visually illustrated in Fig. 5.

As can be seen from Fig. 5, there are relatively significant discrepancies between the experimental data and theory results in low-energy channels. This is mainly attributed to practical experimental imperfections such as optical path alignment errors and optical losses. The interference of experimental errors on the analysis results is particularly prominent in low SNR regions, leading to greater uncertainty in the measured data of low-energy channels compared to high-energy channels. For the dominant channels with higher energy in the OAM spectrum, from a theoretical perspective, their expected energy projection ratio should be 1:1, while our experimental measurements do not show a strictly 1:1 energy projection ratio. This is primarily because the phase layers used in our experiment were designed based on simulations that already have certain measurement deviations for some inputs. Furthermore, as noted earlier, practical imperfections in the experimental setup introduce additional channel crosstalk. Nevertheless, the overall results still demonstrate a projection ratio that closely approximates the theoretical value. We can further improve the measurement accuracy of the OAM spectrum by increasing the number of layers to suppress this channel crosstalk.

To provide a clearer representation of the measurement error of our sorting device for the OAM spectrum, we use fidelity to quantify the agreement between the output channel energy of the corresponding OAM state and the intended target:

$$P_{\mathrm{Sim/Exp}}^m = \frac{G_{\mathrm{Theory}}^m \left(G_{\mathrm{Sim/Exp}}^m\right)^T}{|G_{\mathrm{Theory}}^m||G_{\mathrm{Sim/Exp}}^m|} \times 100\%, \tag{13}$$

where G_{Theory}^m and $G_{\mathrm{Sim/Exp}}^m$ are a 1×8 row vector comprising the theoretical and experimental (simulated) optical intensity values from the eight target detection regions on the output plane when

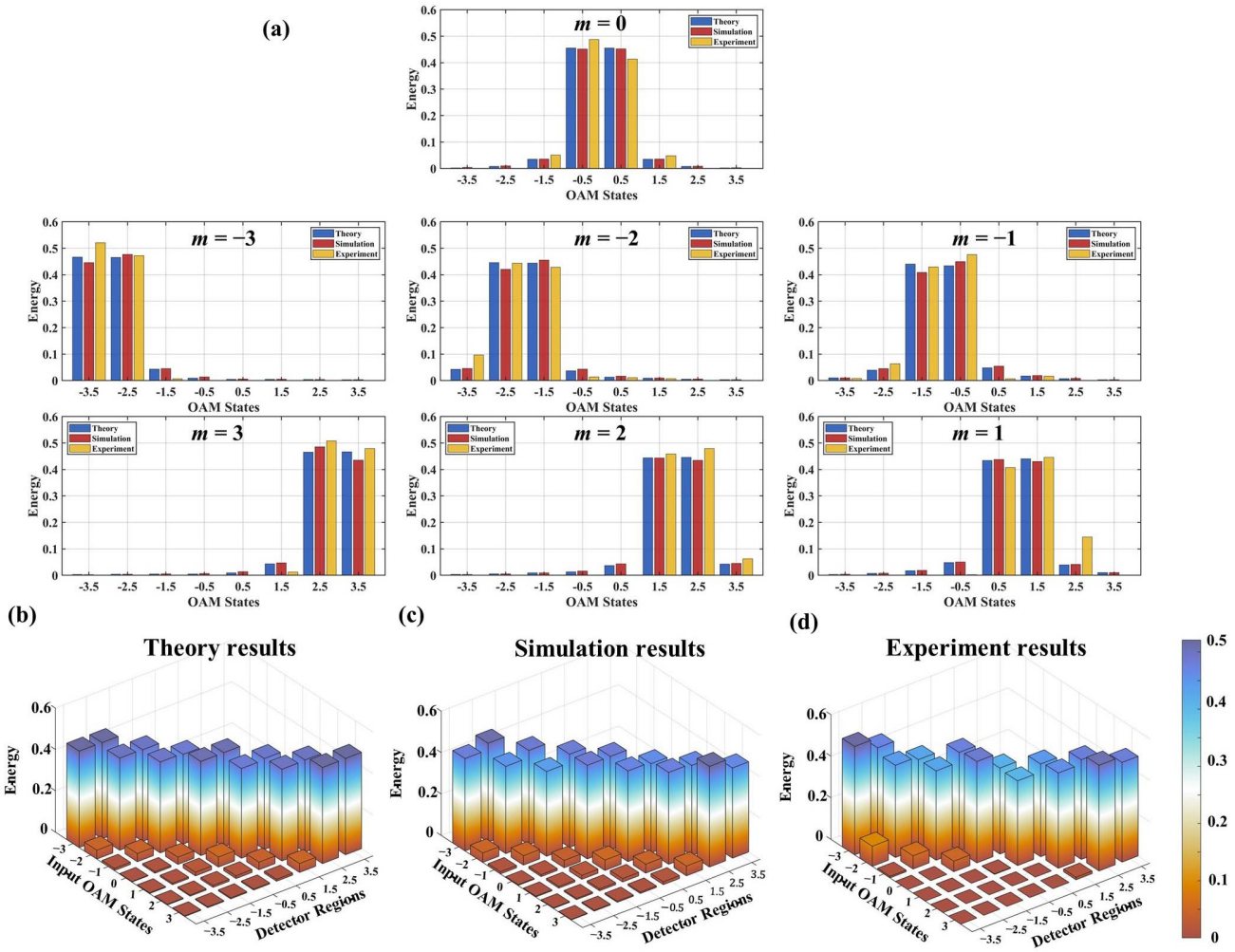

Fig. 5. OAM spectrum at the output plane when different vortex beams are input, with $l = -3.5$ to 3.5 as the orthogonal basis. (a) Comparison of normalized energy histograms among theory, simulation, and experimental outputs. (b) and (c) depict the theory and simulated OAM spectra, while (d) represents the experimentally measured OAM spectra captured and processed by the CCD.

an mth-order OAM vortex beam is used as the input. The calculated fidelity is shown in Table 1. Due to practical noise and device imperfections, the experimental fidelity is slightly lower than theoretical predictions. Nevertheless, it remains consistently high at ~99%, fully meeting the requirements for precise OAM characterization. This remarkable accuracy underscores the excellent performance of our measurement approach. Future improvements, such as employing detectors with higher resolution and sensitivity alongside low-scattering optical lenses, are expected to further reduce losses and distortions, thereby pushing the accuracy of OAM spectrum measurements even closer to the theoretical limit. This capability of precise OAM spectrum measurement can further enhance the discrimination ability of the proposed scheme for adjacent FVBs modes. Details are provided in Note 5 of the Supplementary Material.

Table 1. Fidelity of OAM Spectrum Measurement in Simulation and Experiment.

	$m = -3$	$m = -2$	$m = -1$	$m = 0$	$m = 1$	$m = 2$	$m = 3$
P^m_{sim}	99.94%	99.90%	99.84%	100%	99.99%	99.98%	99.84%
P^m_{Exp}	99.71%	99.53%	99.54%	99.60%	98.14%	99.74%	99.82%

5. Conclusion

In summary, we propose a rapid sorting method for FVBs based on DONN. It provides, for the first time, physical evidence that high-fidelity wavefront deconstruction and sorting can be achieved for complex optical fields such as FVBs with the DONN. By designing the phase parameters of the neurons in the diffractive layers, we establish a precise one-to-one correspondence between the input vortex light and the Gaussian beams at different detection positions on the output plane. This correspondence enables accurate sorting of input vortex light. The results demonstrate that, after training, the network exhibits highly precise and rapid sorting capabilities for both single-mode and multimode FVBs. Additionally, our sorting method shows minimal energy crosstalk between different channels on the output plane, which is less than −20 dB in simulation and less than −10 dB in experiment. We also accurately measured the OAM spectrum with our system, achieving a precision of 99%. Furthermore, we have fully utilized the excellent parallel processing capabilities of the DONN to achieve precise sorting of multi-wavelength FVBs. To verify the practical application effectiveness of the designed sorting device, we constructed a corresponding experimental setup and obtained results that are in complete agreement with the simulation predictions for different inputs. Future research will focus on exploring the robustness and adaptability of this method in complex dynamic and non-ideal environments, with the aim of advancing its practical application. We believe that this rapid, accurate, and flexible sorting method will exhibit significant application potential in fields such as optical communication, and the outstanding parallel processing capabilities demonstrated by our multi-wavelength sorting approach will lay a relevant foundation for future multidimensional multiplexing.

Acknowledgements

This work was supported by the National Natural Science Foundation of China (Nos. 12274105, 12574336, 12574414, 12504380, and 12504438), the China Postdoctoral Science Foundation (Nos. 2025M774294 and 2025M784343), and the Natural Science Foundation of Heilongjiang Province (No. LH2023A006).

References

1. L. Allen, M. W. Beijersbergen, R. J. C. Spreeuw, *et al.*, "Orbital angular momentum of light and the transformation of Laguerre-Gaussian laser modes," Phys. Rev. A **45**, 8185 (1992).
2. Y. Shen, X. Wang, Z. Xie, *et al.*, " Optical vortices 30 years on: OAM manipulation from topological charge to multiple singularities," Light Sci. Appl. **8**, 90 (2019).
3. J. Wang, J.-Y. Yang, I. M. Fazal, *et al.*, "Terabit free-space data transmission employing orbital angular momentum multiplexing," Nat. Photonics **6**, 488 (2012).
4. C. Martin, K. Peuntinger, P. Günthner, *et al.*, "Free-space propagation of high-dimensional structured optical fields in an urban environment," Sci. Adv. **3**, e1700552 (2017).
5. J. Wang, J. Liu, S. Li, *et al.*, "Orbital angular momentum and beyond in free-space optical communications," Nanophotonics **11**, 645 (2022).
6. Y. Guo, Y. Jiang, J. Gao, *et al.*, "Dispersion-managed mode-locking in an all-fiber Er-doped fiber laser with OAM output based on mode superposition," Chin. Opt. Lett. **23**, 111401 (2025).
7. E. E. Elsayed, "Atmospheric turbulence mitigation of MIMO-RF/FSO DWDM communication systems using advanced diversity multiplexing with hybrid N-SM/OMI M-ary spatial pulse-position modulation schemes," Opt. Commun. **562**, 130558 (2024).
8. B. B. Yousif and E. E. Elsayed, "Performance enhancement of an orbital-angular-momentum-multiplexed free-space optical link under atmospheric turbulence effects using spatial-mode multiplexing and hybrid diversity based on adaptive MIMO equalization," IEEE Access **7**, 84401 (2019).
9. Z. Jin, D. Janoschka, J. Deng, *et al.*, "Phyllotaxis-inspired nanosieves with multiplexed orbital angular momentum," eLight **1**, 5 (2021).
10. D. G. Grier, "A revolution in optical manipulation," Nature **424**, 810 (2003).
11. Z. Hao, S. Zhu, C.-W. Qiu, *et al.*, "Vortex localization and OAM selective conversion via cylindrical metagratings," Chin. Opt. Lett. **22**, 033601 (2024).
12. X. Tang, N. Liu, S. Liu, *et al.*, "Tunable autofocus and unconventional OAM through dislocation in superimposed swallowtail vortex beams," Chin. Opt. Lett. **23**, 102602 (2025).
13. H. Zhang, X. Li, H. Ma, *et al.*, "Grafted optical vortex with controllable orbital angular momentum distribution," Opt. Express **27**, 22930 (2019).
14. P. S. Tan, X.-C. Yuan, G. H. Yuan, *et al.*, "High-resolution wide-field standing-wave surface plasmon resonance fluorescence microscopy with optical vortices," Appl. Phys. Lett. **97**, (2010).
15. S. Wei, T. Lei, L. Du, *et al.*, "Sub-100 nm resolution PSIM by utilizing modified optical vortices with fractional topological charges for precise phase shifting," Opt. Express **23**, 30143 (2015).
16. W. Long, J. Pan, X. Guo, *et al.*, "Optimized weak measurement of orbital angular momentum-induced beam shifts in optical reflection," Photon. Res. **7**, 1273 (2019).
17. X. Wang, S. Yu, S. Liu, *et al.*, "Deterministic generation of large-scale hyper-entanglement in three degrees of freedom," Adv. Photonics Nexus **1**, 016002 (2022).
18. Y. Lou, Y. Lv, J. Wang, *et al.*, "Orbital angular momentum multiplexed deterministic all-optical quantum erasure-correcting code," Phys. Rev. Lett. **132**, 040601 (2024).
19. C. Wang, Y. Chen, and L. Chen, "Four-dimensional orbital angular momentum Bell-state measurement assisted by the auxiliary polarization and path degrees of freedom," Opt. Express **30**, 34468 (2022).
20. S. H. Tao, X.-C. Yuan, J. Lin, *et al.*, "Fractional optical vortex beam induced rotation of particles," Opt. Express **13**, 7726 (2005).
21. C.-S. Guo, Y.-N. Yu, and Z. Hong, "Optical sorting using an array of optical vortices with fractional topological charge," Opt. Commun. **283**, 1889 (2010).
22. R. Dasgupta, S. Ahlawat, R. S. Verma, *et al.*, "Optical orientation and rotation of trapped red blood cells with Laguerre-Gaussian mode," Opt. Express **19**, 7680 (2011).
23. G. Situ, G. Pedrini, and W. Osten, "Spiral phase filtering and orientation-selective edge detection/enhancement," J. Opt. Soc. Am. A **26**, 1788 (2009).
24. J. Wang, W. Zhang, Q. Qi, *et al.*, "Gradual edge enhancement in spiral phase contrast imaging with fractional vortex filters," Sci. Rep. **5**, 15826 (2015).
25. H. Liu, Y. Wang, J. Wang, *et al.*, "Electromagnetic vortex enhanced imaging using fractional OAM beams," IEEE Antennas Wirel. Propag. Lett. **20**, 948 (2021).
26. Z. Xu, C. Gui, S. Li, *et al.*, "Fractional orbital angular momentum (OAM) free-space optical communications with atmospheric turbulence assisted by MIMO equalization," in *Photonic Networks and Devices* (Optica Publishing Group, 2014), paper JT3A.1.
27. Y. Zhao, X. Zhong, G. Ren, *et al.*, "Capacity of arbitrary-order orbital angular momentum multiplexing system," Opt. Commun. **387**, 432 (2017).
28. I. Moreno, J. A. Davis, B. M. L. Pascoguin, *et al.*, "Vortex sensing diffraction gratings," Opt. Lett. **34**, 2927 (2009).
29. N. Zhang, X. C. Yuan, and R. E. Burge, "Extending the detection range of optical vortices by Dammann vortex gratings," Opt. Lett. **35**, 3495 (2010).
30. G. C. G. Berkhout, M. P. J. Lavery, J. Courtial, *et al.*, "Efficient sorting of orbital angular momentum states of light," Phys. Rev. Lett. **105**, 153601 (2010).

31. Y. Wen, I. Chremmos, Y. Chen, *et al.*, "Spiral transformation for high-resolution and efficient sorting of optical vortex modes," Phys. Rev. Lett. **120**, 193904 (2018).
32. W. Zhang, Q. Qi, J. Zhou, *et al.*, "Mimicking Faraday rotation to sort the orbital angular momentum of light," Phys. Rev. Lett. **112**, 153601 (2014).
33. Y. Guo, S. Zhang, M. Pu, *et al.*, "Spin-decoupled metasurface for simultaneous detection of spin and orbital angular momenta via momentum transformation," Light Sci. Appl. **10**, 63 (2021).
34. Y. Bao, F. Nan, J. Yan, *et al.*, "Observation of full-parameter Jones matrix in bilayer metasurface," Nat. Commun. **13**, 7550 (2022).
35. J. Hu, D. Mengu, D. C. Tzarouchis, *et al.*, "Diffractive optical computing in free space," Nat. Commun. **15**, 1525 (2024).
36. S. Zarei and A. Khavasi, "Realization of optical logic gates using on-chip diffractive optical neural networks," Sci. Rep. **12**, 15747 (2022).
37. X. Lin, Y. Rivenson, N. T. Yardimci, *et al.*, "All-optical machine learning using diffractive deep neural networks," Science **361**, 1004 (2018).
38. Z. Huang, P. Wang, J. Liu, *et al.*, "All-optical signal processing of vortex beams with diffractive deep neural networks," Phys. Rev. Appl. **15**, 014037 (2021).
39. J. Zhang, Z. Ye, J. Yin, *et al.*, "Polarized deep diffractive neural network for sorting, generation, multiplexing, and de-multiplexing of orbital angular momentum modes," Opt. Express **30**, 26728 (2022).
40. W. Xiong, Z. Huang, P. Wang, *et al.*, "Optical diffractive deep neural network-based orbital angular momentum mode add–drop multiplexer," Opt. Express **29**, 36936 (2021).
41. Q. Jia, Y. Zhang, B. Shi, *et al.*, "Simultaneously sorting vector vortex beams of 120 modes," Nanophotonics **12**, 3955 (2022).
42. X. Li, R. Feng, F. Sun, *et al.*, "Simultaneous sorting of arbitrary vector structured beams with spin-multiplexed diffractive metasurfaces," Adv. Photonics Nexus **3**, 036010 (2024).
43. S. Ren, Q. Jia, and W. Ding, "Simultaneously sorting of fractional vortex beams (FVBs) based on diffractive optical neural network," in *IEEE Academic International Symposium on Optoelectronics and Microelectronics Technology* (2024), p. 335.
44. Q. Jia, B. Shi, Y. Zhang, *et al.*, "Partially coherent diffractive optical neural network," Optica **11**, 1742 (2024).
45. J. W. Goodman, *Introduction to Fourier Optics* (Springer, 2017).
46. Y. Yang, A. Forbes, and L. Cao, "A review of liquid crystal spatial light modulators: devices and applications," Opto-Electron. Sci. **2**, 230026 (2023).
47. L. Huang, Y. Cao, S. Ren, *et al.*, "Optical computational imaging through unknown random diffusers in visible spectrum," Laser Photonics Rev. e01168 (2025).
48. S. Buckley, A. N. Tait, A. N. McCaughan, *et al.*, "Photonic online learning: a perspective," Nanophotonics **12**, 833 (2023).
49. Z. Xue, T. Zhou, Z. Xu, *et al.*, "Fully forward mode training for optical neural networks," Nature **632**, 280 (2024).
50. T. Zhou, L. Fang, T. Yan, *et al.*, "*In situ* optical backpropagation training of diffractive optical neural networks," Photon. Res. **8**, 940 (2020).
51. J. Feng, H. Chen, D. Yang, *et al.*, "Multi-wavelength diffractive neural network with the weighting method," Opt. Express **31**, 33113 (2023).
52. Z. Duan, H. Chen, and X. Lin, "Optical multi-task learning using multi-wavelength diffractive deep neural networks," Nanophotonics **12**, 893 (2023).